

Research Article

Open Access



A property-oriented self-decision design strategy of low-alloyed rare earth-free magnesium alloys with a good strength-ductility synergy based on machine learning

Xu Qin¹, Qinghang Wang^{1*}, Xinqian Zhao¹, Shouxin Xia¹, Li Wang¹, Jiabao Long¹, Yuhui Zhang², Bin Jiang^{3,*}

¹School of Mechanical Engineering, Yangzhou University, Yangzhou 225127, Jiangsu, China.

²School of Materials Science and Engineering, Xiamen University of Technology, Xiamen 361024, Fujian, China.

³National Engineering Research Center for Magnesium Alloys, College of Materials Science and Engineering, Chongqing University, Chongqing 400044, China.

*Correspondence to: Prof. Qinghang Wang, School of Mechanical Engineering, Yangzhou University, No. 196 Huayang West Road, Yangzhou 225127, Jiangsu, China. E-mail: wangqinghang@yzu.edu.cn; Prof. Bin Jiang, National Engineering Research Center for Magnesium Alloys, College of Materials Science and Engineering, Chongqing University, No. 174 Shazheng Street, Shapingba District, Chongqing 400044, China. E-mail: jiangbinrong@cqu.edu.cn

How to cite this article: Qin, X.; Wang, Q.; Zhao, X.; Xia, S.; Wang, L.; Long, J.; Zhang, Y.; Jiang, B. A property-oriented self-decision design strategy of low-alloyed rare earth-free magnesium alloys with a good strength-ductility synergy based on machine learning. *J. Mater. Inf.* 2025, 5, 13. <https://dx.doi.org/10.20517/jmi.2024.92>

Received: 23 Dec 2024 **First Decision:** 22 Jan 2025 **Revised:** 25 Jan 2025 **Accepted:** 6 Feb 2025 **Published:** 22 Feb 2025

Academic Editor: Yong Du **Copy Editor:** Pei-Yun Wang **Production Editor:** Pei-Yun Wang

Abstract

Machine learning (ML) is revolutionizing alloy design, yet traditional models face challenges with limited data and complex nonlinearities. Our study presents a self-decision design strategy that integrates target property determination, reverse and forward modeling, and feature importance analysis to optimize low-alloyed rare earth (RE)-free magnesium alloys for strength-ductility synergy. The strategy was validated with experimental data, leading to the development of a new Mg-2Al-1Zn-0.6Ca-0.4Mn (wt%) alloy processed at specific conditions, achieving a tensile strength of 344 MPa and an elongation-to-failure (EL) of 21.3% at room temperature. The discrepancies between experimental and predicted results were less than 5%, underscoring the accuracy of this approach. This streamlined design strategy not only promises to accelerate the development of low-cost, high-performance alloys but also minimizes the need for human intervention, thereby enhancing the efficiency and precision of alloy design.

Keywords: Magnesium alloy, machine learning, self-decision, microstructure, strength-ductility synergy



© The Author(s) 2025. **Open Access** This article is licensed under a Creative Commons Attribution 4.0 International License (<https://creativecommons.org/licenses/by/4.0/>), which permits unrestricted use, sharing, adaptation, distribution and reproduction in any medium or format, for any purpose, even commercially, as long as you give appropriate credit to the original author(s) and the source, provide a link to the Creative Commons license, and indicate if changes were made.



INTRODUCTION

Magnesium (Mg) alloys have been widely used in the automobile field and aerospace industry due to low density and high specific strength/stiffness^[1,2]. However, high-performance Mg alloys often tend to be required to add high-content and expensive alloying elements [e.g., rare earth (RE)] for enhancing their mechanical properties^[3-5], which significantly increases the production costs and negatively affects the recycling and environmental protection. Therefore, it is urgent to develop low-alloyed free-RE Mg alloys with high mechanical properties, which has gradually become a hot-point research direction in the field of metallic materials.

In recent years, low-alloyed high-performance Mg-Al-Ca-Mn-(Zn) alloys have gained increasing attention. Unlike high-alloyed RE-containing Mg alloys, improving the strength of these low-alloyed Mg alloys through aging precipitation is challenging. For instance, the precipitation strengthening increment in Mg-Gd/Y alloys can reach 143 MPa^[6,7], while in low-alloy Mg alloys, the effect is typically less than 50 MPa^[8-10]. Li *et al.* reported that the peak-aged Mg-1.5Al-0.3Ca-0.4Mn-1.5Zn (wt%) alloy exhibited only an increase of 38 MPa in tensile yield strength (TYS) compared to its solid-solution-treated counterpart, showing the limitations of precipitation strengthening in low-alloyed Mg alloys^[10].

Nevertheless, significant grain refinement strengthening effect, mainly due to high k -value (Hall-Petch slope), provides an opportunity for the design of high-strength low-alloyed Mg alloys. Low-temperature deformation is a cost-effective and potential approach to introducing numerous (ultra-) fine grains^[11-13]. As an example, Liu *et al.* produced a highly strong and ductile Mg-1.0Al-1.0Ca-0.4Mn (wt%) alloy with an ultimate tensile strength (UTS) of 419 MPa and an elongation-to-failure (EL) of 12% because of an ultra-fined grain structure (average grain size of 0.43 μm) after low-temperature extrusion at 200 $^{\circ}\text{C}$ ^[13].

Besides, hetero-structures (i.e., bi-modal, gradient, and layered structures^[14-16]) show great potential for obtaining superior mechanical properties in Mg alloys, due to the formation of back stress. For instance, Zhang *et al.* found that an as-extruded Mg-1Mn-0.5Al-0.5Ca (wt%) alloy with a bimodal grain structure containing fine grains (1 μm) and coarse grains (20-40 μm) exhibited a TYS of 360 MPa and an EL of 11%, while the homogeneous structured alloy only attained a TYS of 151 MPa and an EL of 8% owing to a lack of hetero-deformation induced (HDI) effect^[14].

As mentioned above, low-alloyed Mg-Al-Ca-Mn-(Zn) alloys hold great potential to achieve a good strength-ductility synergy. However, researchers also have found it challenging to quickly and accurately design Mg alloys that meet multiple performance requirements through traditional trial-and-error methods. With the rapid development of materials science and artificial intelligence technology, new research paradigms based on data-driven and computational materials science are gradually replacing the traditional trial-and-error approach. Machine learning (ML) methods can design high-performance materials in unknown spaces by extracting hidden relationships between compositions, processing parameters, and properties. In recent years, researchers have used ML-based models to design various high-performance alloys^[17-20], such as high-strength steel, high-strength-conductivity copper alloys and high-strength-stress corrosion resistance aluminum alloys. For example, Lee *et al.* designed a medium-manganese steel with a UTS of 1,957 MPa and an EL of 10.7% using a boosted decision tree (DT) regression model^[17]. Yuan *et al.* proposed a stacking multi-algorithm model to design four high strength-toughness as-extruded 7xxx alloys achieving UTS of 709 MPa and EL of 16%, compared to traditional processing methods^[19]. However, these methods typically require an exhaustive multidimensional search, which is both complex and time-consuming. More promising is the development of self-decision design models capable of rapidly identifying optimal combinations of compositions and processing parameters based on target properties

with minimal human intervention.

The purpose of this study is to propose a property-oriented self-decision design (POSDD) strategy for optimizing low-alloyed RE-free Mg alloys with good strength-ductility synergy. This strategy represents a significant advancement in the field of materials science. It amalgamates several critical components: the determination of target properties, the construction of reverse and forward models, and a feature importance analysis-assisted screening process. These elements are synergistically employed to identify novel compositions and processing parameters for low-alloyed RE-free Mg alloys, specifically those within the Mg-Al-Ca-Mn-(Zn) system, which exhibit an optimal balance between strength and ductility.

MATERIALS AND METHODS

The methodology for the design of high-performance, low-alloyed RE-free Mg alloys, as delineated in this study, is systematically presented in [Figure 1](#). The process was structured into three distinct yet interrelated stages: data preparation, application of the POSDD strategy, and experimental validation.

The initial stage involved the compilation and refinement of a standardized dataset encompassing Mg alloys with elements such as Al, Ca, Mn, and Zn. This dataset was meticulously processed through a data enhancement approach to ensure its quality and reliability for subsequent analysis.

Subsequently, the POSDD strategy was meticulously formulated and deployed to deduce the alloy compositions and processing parameters that were predicted to yield the desired mechanical properties. This strategy leveraged advanced computational techniques to optimize the alloy design, thereby streamlining the development process.

The final stage entailed experimental validation of the alloys shortlisted by the POSDD strategy. This involved a thorough comparison of the mechanical properties predicted by the model with those obtained from actual experiments. Additionally, the underlying strengthening and plasticity mechanisms were analyzed to provide a deeper understanding of high-performance Mg alloys.

Data preparation

Data sources

The dataset employed in this study was derived from published experimental data on Mg alloys that incorporate Al, Zn, Ca, and Mn. The dataset comprises 233 entries, with each variable visualized through violin plots as illustrated in [Figure 2](#). The data were systematically organized into three main categories: alloying elements (Al, Zn, Ca, and Mn), processing parameters [solution treatment temperature (ST), solution treatment time (St), extrusion temperature (ET), extrusion speed (ES), and extrusion ratio (ER)], and mechanical properties (UTS and EL).

In terms of alloy composition, the weight percentages of Al, Zn, Ca, and Mn were distributed from 0% to 9%, 0% to 9%, 0% to 5%, and 0% to 3%, respectively. ST and St were distributed from 200 to 550 °C and 0 to 60 h, respectively. ET ranged from 50 to 500 °C, ES from 0.1 to 60 m/min, and ER from 10 to 80. UTS and EL were distributed over a range of 150 to 400 MPa and 1% to 50%, respectively. This comprehensive dataset serves as a solid foundation for analyzing the interplay between alloy composition, processing parameters, and mechanical properties, thereby enabling the development of a predictive model with enhanced accuracy and dependability.

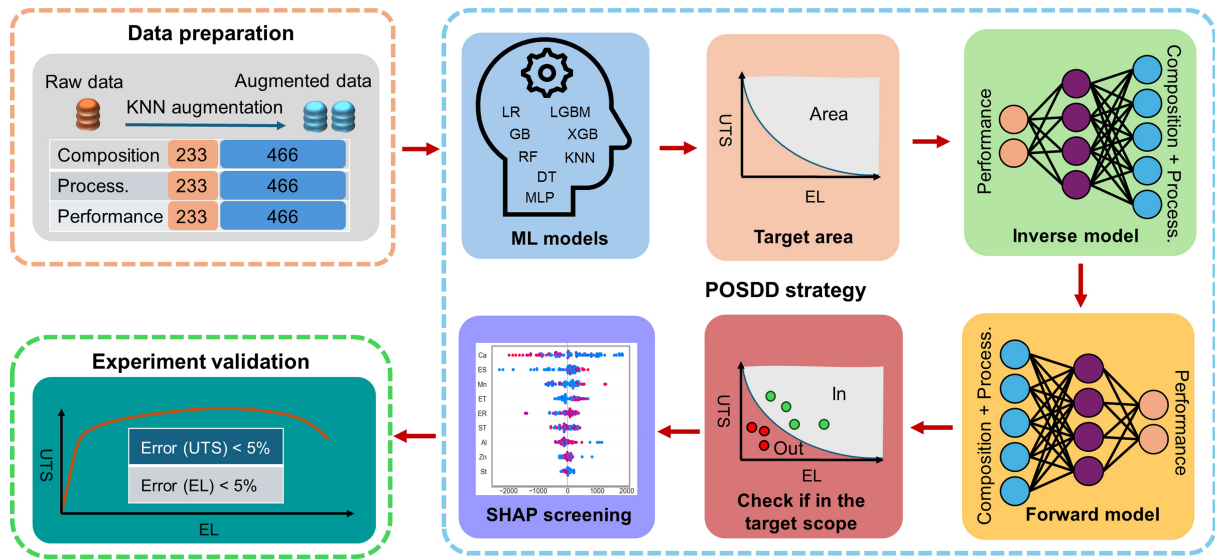


Figure 1. POSDD strategy for high-performance low-alloyed Mg alloys. POSDD: Property-oriented self-decision design.

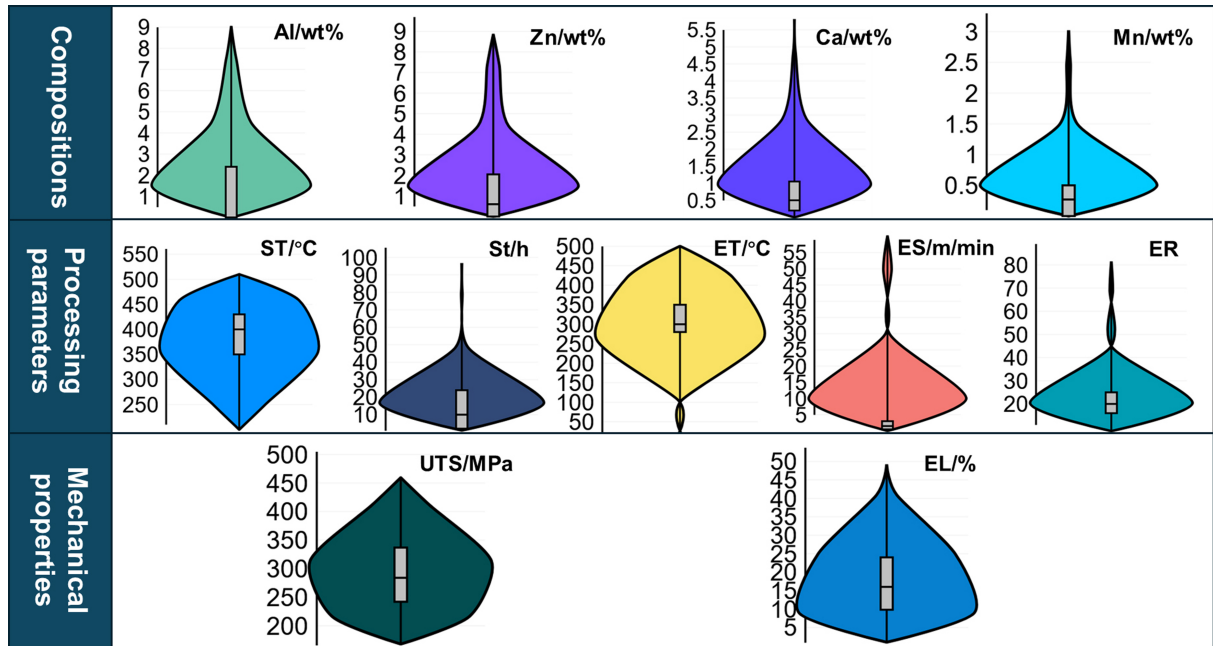


Figure 2. Data distribution including alloy compositions (Al, Zn, Ca, and Mn), processing parameters (ST, St, ET, ES, and ER), and mechanical properties (UTS and EL). ST: Solution treatment temperature; St: solution treatment time; ET: extrusion temperature; ES: extrusion speed; ER: extrusion ratio; UTS: ultimate tensile strength; EL: elongation-to-failure.

Data augmentation

In an effort to bolster the quality of the dataset and, consequently, the robustness of the ML model, this study implemented a data augmentation technique predicated on K-nearest neighbor (KNN) interpolation. The KNN interpolation technique improves the dataset quality by filling gaps in the data distribution, thereby ensuring better coverage of the feature space. By generating new data points based on the proximity of existing ones, KNN creates a more comprehensive and balanced dataset. Recognized for its efficacy in sample data generation, the KNN method leveraged the relationships among similar samples within the

dataset, which not only enhances the dataset's integrity but also fortifies the model's ability to generalize from the training data to unseen samples, ensuring a more reliable and accurate ML model predictive performance.

A key advantage of KNN interpolation lies in its flexibility. By adjusting the K -value (i.e., the number of nearest neighbors), the interpolation range and the diversity of new samples can be precisely controlled, making it adaptable to various datasets. This method not only significantly expands the training set but also effectively improves the model's generalization ability.

The original dataset was set as $X = \{x_1, x_2, \dots, x_n\}$, where each x_i is a multidimensional feature vector. The query point was located among its k nearest neighbors, denoted as $N_k(q) = \{x_{i_1}, x_{i_2}, \dots, x_{i_m}\}$, based on the fact that the weighted average of the k neighbors is the result of interpolation, the KNNs are interpolated to generate enhanced data x' , as given in^[21]:

$$x' = \frac{\sum_{j=1}^k (w_j \cdot x_{i_j})}{\sum_{j=1}^k (w_j)} \quad (1)$$

where w_j is the weight of the j -th nearest neighbor. x_{i_j} is the value of the j -th nearest neighbor. Specifically, the augmented data x' is obtained by multiplying the value of each nearest neighbor point by its corresponding weight, then summing it up and finally dividing it by the sum of all weights. This method not only preserves the core features of the original data, but also introduces moderate variations, thus generating high-quality augmented data.

POSDD strategy

Target property determination

In the realm of target property determination, conventional methodologies often adhere to the establishment of a singular, fixed target property value. Deviating from this norm, the present study introduced a novel approach within the POSDD strategy, wherein a target region, denoted as A , was dynamically selected through a self-decision mechanism, as depicted in [Figure 3](#). This methodological shift allows for a more flexible and nuanced definition of the target property, which is better aligned with the complex and multifaceted nature of alloy design. The process of plotting the Pareto frontier F for the current dataset^[22], which represents the optimal set of solutions that are non-dominated with respect to the considered properties, was executed in a two-step procedure as follows:

For any point (EL, UTS) in the dataset, if there is no other point (EL', UTS') that satisfied

$$EL' \geq EL \text{ and } UTS' \geq UTS \quad (2)$$

the point (EL, UTS) is considered non-dominated (not surpassed by any other point). Next, all these non-dominated points form the Pareto frontier F , which can be defined as:

$$F = \{(EL, UTS) / \nexists (EL', UTS')\} \quad (3)$$

The points on the Pareto frontier form the optimal point set, as shown in [Table 1](#). The region in the upper right of the Pareto frontier was considered as the target performance point. The points in this target area A were represented as:

Table 1. Optimal points of the Pareto frontier

EL (%)	UTS (MPa)	EL (%)	UTS (MPa)
10	459	21	329
10.7	437	23	325
12	419	24	320
13.2	396	25	309
13.3	358.5	28.3	300
14.2	350	29.9	294
14.4	349	34	273
16	340	36.7	240.1
18.1	337.6	37	240
20	332	44	210

EL: Elongation-to-failure; UTS: ultimate tensile strength.

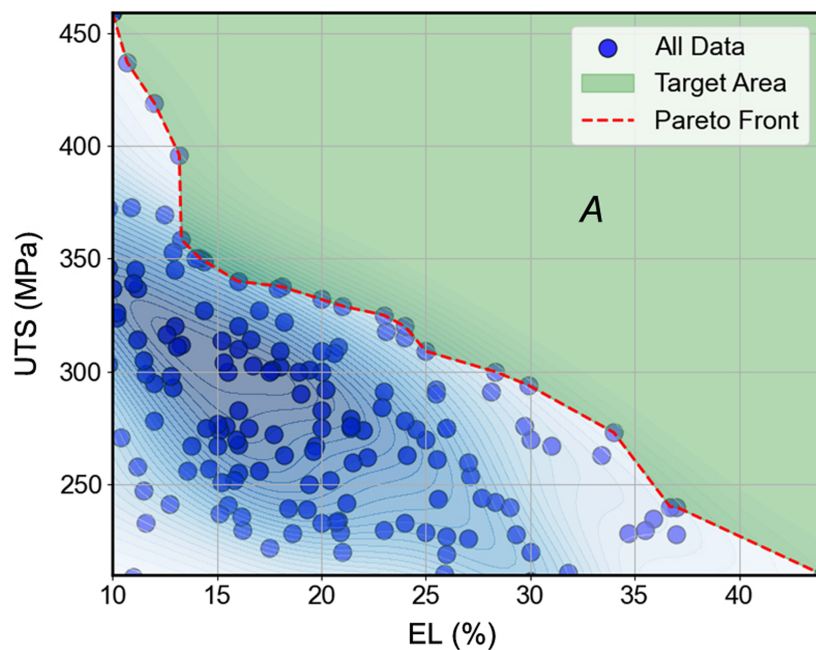


Figure 3. Determination of target property area.

$$UTS_{\text{Pareto}}(EL) \leq UTS \leq UTS_{\text{max}} \quad (4)$$

$$EL_{\text{min}} \leq EL \leq EL_{\text{max}} \quad (5)$$

where $UTS_{\text{Pareto}}(EL)$ represents the set of optimal points. UTS_{max} is the maximum UTS corresponding to the Pareto frontier. EL_{min} and EL_{max} represent the minimum and maximum values of EL corresponding to the Pareto frontier, respectively. Once this range was established, randomly generated data points within the range were used as inputs to the inverse design model.

Model building

Eight ML models [including linear regression (LR), DT, random forest (RF), gradient boosting (GB), KNN, XGBoost (XGB), multi-layer perceptron (MLP), and light gradient boosting machine (LGBM)] were

evaluated for their efficiency in constructing the forward and reverse models. The model performance was assessed using the coefficient of determination (R^2) as follows^[19]:

$$R^2 = 1 - \frac{\sum_{i=1}^m (y_i - \hat{y}_i)^2}{\sum_{i=1}^m (y_i - \bar{y}_i)^2} \quad (6)$$

where y_i represents the true values; \hat{y}_i represents the model's predicted values; \bar{y}_i represents the mean of all true values, and m is the number of samples.

The beginning of our study involved the deployment of a reverse model, which was tasked with predicting the compositions and processing parameters of the alloy based on the desired mechanical properties. However, upon encountering limitations in the predictive accuracy of the reverse model, a synergistic approach was adopted, integrating both the reverse and forward modeling techniques. This combined strategy was designed to harness the strengths of both methodologies, thereby enhancing the overall predictive power of the system. In this refined approach, the reverse model was utilized to generate a spectrum of potential compositions and processing parameters. These candidate solutions were then systematically input into the forward model, which was responsible for predicting the corresponding mechanical properties. This dual-model strategy allowed for a comprehensive assessment of the accuracy of the reverse model's predictions by comparing the forward model's output against the actual mechanical properties.

Based on the model performance evaluation, the models with the highest prediction accuracy were selected as the core algorithms. During the training, the augmented Mg alloy dataset was randomly divided into training and testing sets in a ratio of 4:1 and evaluated using five-fold Cross-Validation ($CV = 5$). Specifically, the model was trained five times, using four parts as the training set and the remaining part as the testing set in each iteration. The final result was taken as the average of five modeling results. In order to further reduce the fluctuation of model performance due to differences in data partitioning, ten rounds of randomized $CV = 5$ were conducted, and the average result of these ten rounds was used as the final evaluation metric. In this way, the fluctuation in prediction caused by the difference in the division of the training set and the testing set could be effectively decreased, and the predictive ability of the model could be more accurately evaluated.

Feature importance analysis assisted screening

Within the confines of the specified target region, a substantial array of alloy compositions and processing parameters was identified. However, the experimental validation of this extensive dataset poses a significant challenge due to the resource-intensive nature of such an endeavor. To navigate this complexity, we integrated the Shapley Additive Explanations (SHAP) method within our feature importance analysis, particularly tailored to the constraints of low-alloying boundary conditions.

Ca content was within the range as follows:

$$0 \leq \text{Ca} \leq 1 \text{ wt\%} \quad (7)$$

Excessive Ca has been found to reduce the EL^[10-16]. Additionally, the total content of alloying elements (Al, Zn, Ca, and Mn) was required as follows:

$$\text{Al} + \text{Zn} + \text{Ca} + \text{Mn} \leq 4 \text{ wt\%} \quad (8)$$

The SHAP having additive and model-agnostic nature enables seamless integration with the self-decision strategy, used to perform a feature importance analysis.

In order to synthesize the two key mechanical property indicators, UTS and EL, the product of both was defined as the combined property index (CPI), which is expressed as follows^[23]:

$$\text{CPI} = \text{UTS} * \text{EL} \quad (9)$$

The specific steps were listed as follows:

(1) Calculation of CPI: The initial step involved the calculation of the CPI for each feature. The SHAP value quantifies the individual contribution of each feature to the model's predictions. These features were then ranked in accordance with the absolute magnitude of their CPI coefficients, providing a metric of their relative influence on the model outcomes.

(2) Selection of Optimal Feature Values: Subsequently, the maximum allowable value was selected for features exhibiting a positive CPI, as these are indicative of a beneficial effect on the target property. Conversely, the minimum allowable value was chosen for features with a negative CPI, as these are associated with an adverse impact. This process ensures that only the values of features that contribute constructively to the desired properties are considered.

(3) Feature Screening and Optimization: Commencing with the feature that demonstrated the highest absolute value of the CPI, a sequential screening process was initiated. Features were assessed in descending order of their importance, as determined by the SHAP ranking. This iterative approach facilitated the identification of the optimal alloy compositions and processing parameters that are most likely to yield the desired mechanical properties.

Experimental validation

Based on the POSDD strategy, a new AZXM2110 alloy was selected to validate the generalization performance of the model. The as-cast alloy was fabricated by gravity casting under mixed gas ($V_{\text{SF}_6}:V_{\text{CO}_2} = 1:99$) atmosphere. The raw materials were commercially pure magnesium ingots ($\geq 99.99\%$), pure aluminum ingots ($\geq 99.9\%$), pure zinc particles ($\geq 99.9\%$), Mg-10Mn (wt%), and Mg-15Ca (wt%) intermediate alloys. The as-cast alloy was homogenized at 400 °C for 11 h and subsequently extruded into bar at 240 °C with an ER of 20 and an ES of 4 m/min by an XJ-500 horizontal extruder.

The microstructures were examined using a scanning electron microscope (SEM, Gemini SEM 300), X-ray diffraction (XRD, Rigaku D/Max 2500), electron backscatter diffraction (EBSD, JEOL JSM-7800 F) and a transmission electron microscope (TEM, FEI TECNAI G2 F20). The area fraction of the secondary phases was measured using Image J software. The tensile samples (a gauge length of 25 mm and a gauge diameter of $\Phi 5$ mm) were machined from the as-extruded alloy along the extrusion direction (ED) and tested using a CMT6305-300 KN universal testing machine at a strain rate of 10^{-3} s^{-1} at room temperature.

RESULTS AND DISCUSSION

Data enhancement

During the data preparation, a comparative analysis is conducted to assess the predictive performance of three distinct datasets: the original dataset, the dataset augmented through interpolation, and the dataset specifically interpolated using the KNN method. This analysis aimed to evaluate the impact of composition and processing parameters on the mechanical properties (UTS and EL), employing a support vector regression (SVR) model, as illustrated in Figure 4. In the context of KNN interpolation, the parameter k was deliberately set to 3, a choice informed by a thorough literature review. This selection is underpinned by the need to achieve a delicate equilibrium between several critical factors: maintaining data diversity, mitigating the introduction of noise, ensuring computational efficiency, and preserving the integrity of the local data structure. The value of $k = 3$ has been demonstrated to effectively balance these competing considerations, thereby optimizing the interpolation process and enhancing the dataset's suitability for accurate mechanical property predictions^[24].

The volume of the dataset is a pivotal factor in shaping the performance of ML models. The initial dataset in this study comprises 233 samples, which serves as the baseline for comparison. In contrast, both the interpolated dataset and the KNN-interpolated dataset have been expanded to 466 samples, effectively doubling the dataset size as depicted in Figure 4A. This augmentation in dataset size is a deliberate strategy to enhance the diversity and coverage of the data, particularly in areas that were previously underrepresented in the original dataset.

The accuracy of a model, as quantified by the R^2 , is significantly enhanced with the employment of interpolated datasets. In the case of the original dataset, the R^2 value for UTS is 0.74, whereas for EL, it is considerably lower at 0.51. This disparity underscores the dataset's inherent limitations in predicting elongation, attributed to its modest size and uneven distribution, as illustrated in Figure 4B. The application of ordinary interpolation techniques yields a notable improvement in R^2 values, with UTS increasing to 0.77 and EL to 0.71. These enhancements underscore the positive impact of data diversity augmentation on the predictive accuracy of the model. The utilization of KNN interpolation further amplifies the performance, achieving an R^2 of 0.82 for UTS and 0.79 for EL. This outcome exemplifies the KNN method's efficacy in achieving a delicate balance between data diversity and noise reduction, thereby enhancing the model's predictive capabilities.

Despite the expansion in dataset size, the training time for all datasets remains commendably efficient, as depicted in Figure 4C. The original dataset requires a mere 0.18 s for training, the interpolated dataset 0.35 s, and the KNN-interpolated dataset 0.28 s, indicating that the interpolation processes do not adversely affect the computational feasibility of the model training, ensuring that the benefits of increased dataset size can be realized without compromising the practicality of the model deployment.

The analysis of the learning curve reveals the superior generalization performance of the KNN-interpolated dataset, as depicted in Figure 4D. The validation error of this dataset decreases from 5,245.96 to 473.56, a significantly lower convergence point compared to the other datasets, indicating an enhanced ability to generalize new, unseen data. The ordinary interpolated dataset follows, with a reduction in validation error from 5,155.01 to 1,115.42, consistently surpassing the original dataset. In contrast, the original dataset exhibits a high initial validation error of 9,331.53, decreasing to 2,799.74, suggesting a lack of diversity and coverage necessary for effective generalization. This adaptability of KNN enhancement gives it a clear advantage over general interpolation, particularly when larger datasets are involved. In the current scenario, with a sample size exceeding 140, KNN-generated data effectively balances diversity and density, enabling

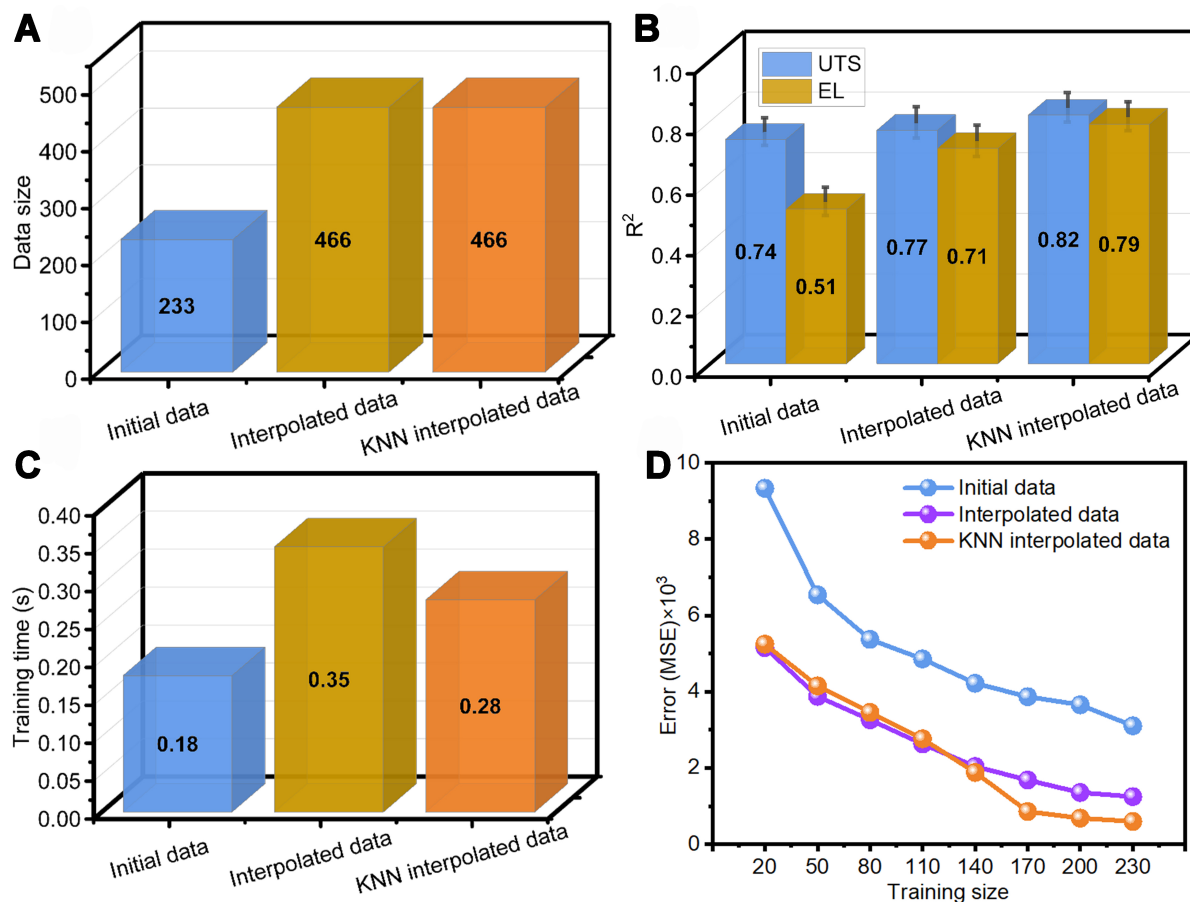


Figure 4. Comparison of the original dataset, the interpolated dataset, and the KNN interpolated dataset: (A) data size; (B) R^2 ; (C) training time; (D) learning curve. KNN: K-nearest neighbor; R^2 : the coefficient of determination.

the model to generalize more effectively and achieve higher prediction accuracy. These findings underscore the efficacy of KNN interpolation in bolstering both data diversity and model generalization.

Model accuracy analysis

In the reverse model, the KNN-augmented dataset was used for training, with UTS and EL as inputs, and alloy composition elements (Al, Zn, Mn, and Ca) and processing parameters (ST, St, ET, ES, and ER) as outputs. The prediction accuracy of the models is illustrated in Figure 5. Figure 5A presents a heat map of the reverse design prediction results, where the horizontal axis represents alloy composition elements, the vertical axis indicates the prediction accuracy of eight models, and the color gradient ranges from red (high accuracy) to blue (low accuracy). Figure 5B-I details the prediction accuracy of each model individually. Among the models, RF model achieves the highest overall R^2 with an average value of 0.37. It performs relatively well in predicting Ca ($R^2 = 0.68$), ET ($R^2 = 0.44$), and ES ($R^2 = 0.46$), making it the optimal model for this task. The superior performance of the RF model can be attributed to its ensemble learning approach, which constructs multiple DTs and combines their outputs, effectively reducing overfitting and improving the model's generalization ability^[25]. The performance of the other models, ranked by average R^2 , is as follows: GB (0.28), LGBM (0.27), XGB (0.21), KNN (0.14), LR (0.09), DT (0.01), and MLP (-0.10).

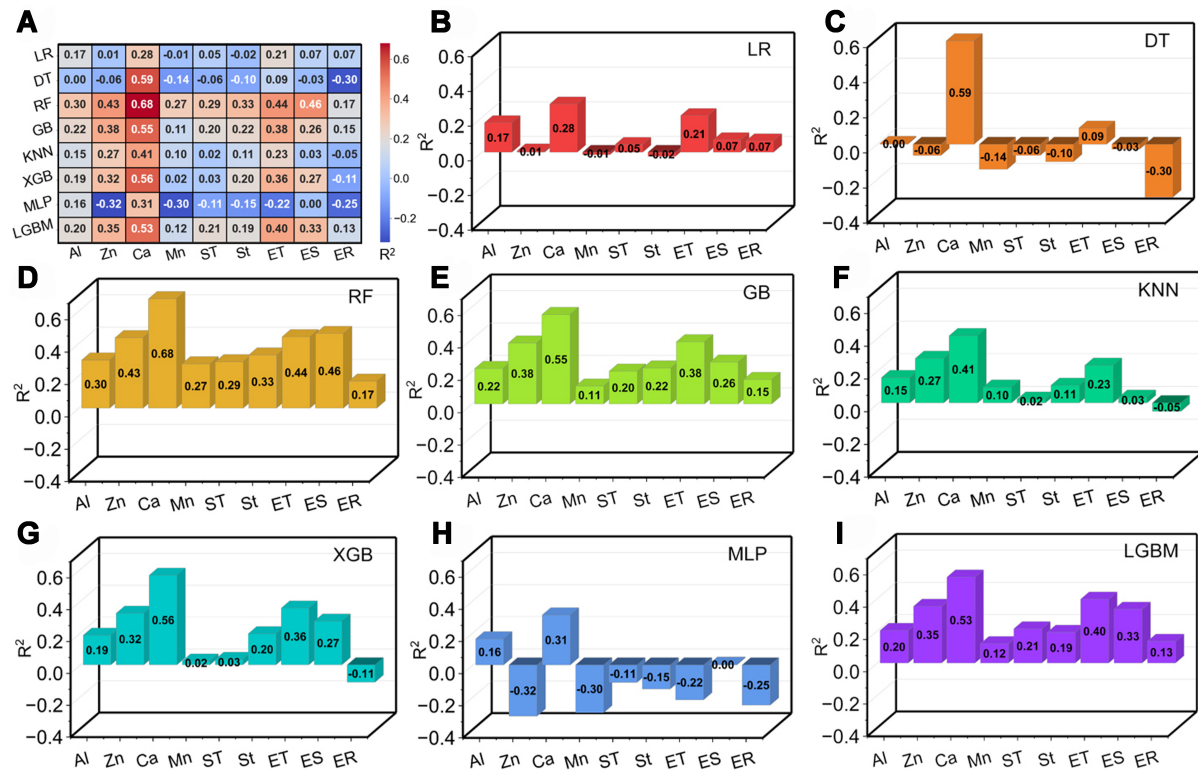


Figure 5. Reverse design prediction performance: (A) overall prediction heat map; (B-I) different models: LR, DT, RF, GB, KNN, XGB, MLP, LGBM, respectively. LR: Linear regression; DT: decision tree; RF: random forest; GB: gradient boosting; KNN: K-nearest neighbor; XGB: XGBoost; MLP: multi-layer perceptron; LGBM: light gradient boosting machine.

It can be seen that the reverse model generally yields low prediction accuracy. This can be attributed to the fact that only two attributes (UTS and EL) were used to predict nine compositions and processing parameters, referred to as “incremental dimensional fit modeling”^[26]. Fitting multiple outputs with fewer input variables often leads to poor model convergence or overfitting, thus reducing the reliability of the model. This suggests that relying solely on the reverse model for compositions and processing parameters design is less dependable.

The results in Table 2 clearly highlight the reverse design model’s limited accuracy in predicting both alloy composition and processing parameters^[27-31]. For instance, in A1 alloy, the experimental values for Al, Ca, and Mn are 3.60, 3.40, and 0.30 wt%, whereas the model predictions are 2.57, 2.94, and 0.19 wt%, respectively. This brings about the prediction errors of 28.6%, 13.5%, and 36.7%, respectively. Similarly, in A5 alloy, the experimental value for Al is 0.61 wt%, but the model predicts 0.04 wt%, leading to an error of 93.4%. For Zn, the experimental value is 0.00 wt%, but the model significantly over-predicts it at 2.12 wt%. Regarding processing parameters, the experimental ES is 3.40 m/min, but the model predicts 5.67 m/min, leading to an error of 66.8%. The experimental validation strongly supports the conclusion that the reverse design model requires further refinement.

In the forward model, the same KNN-augmented dataset was applied for training. The forward model was built using compositions and processing parameters as inputs, and the mechanical properties (UTS and EL) were outputs. The accuracy of the models is shown in Figure 6. Figure 6A and B shows the UTS and EL prediction accuracy, respectively. Among the models, XGB model performs the best, with R^2 of 0.89 and

Table 2. Prediction results of inverse design model in Al-A5 alloys

Alloy	UTS/MPa	EL/%	Category	Al/wt%	Zn/wt%	Ca/wt%	Mn/wt%	ST/°C	St/h	ET/°C	ES/m/min	ER	Ref.
A1	314	9.5	Experiment	3.60	0.00	3.40	0.30	0	0	400	0.12	20	[27]
			Prediction	2.57	0.26	2.94	0.19	413	7	383	0.88	21	
A2	432	7.5	Experiment	3.00	1.00	1.00	0.30	400	24	250	0.10	19	[28]
			Prediction	3.13	0.68	0.94	0.32	453	23	248	0.11	19	
A3	284	22.9	Experiment	3.00	1.00	0.50	0.30	400	6	300	1.00	9	[29]
			Prediction	1.75	1.84	0.42	0.37	364	9	295	1.26	15	
A4	314	16.6	Experiment	4.00	0.00	2.00	0.40	0	0	350	9.40	12	[30]
			Prediction	2.94	0.10	1.72	0.44	370	9	328	6.19	16	
A5	250	19.4	Experiment	0.61	0.00	0.46	0.00	400	24	400	3.40	28	[31]
			Prediction	0.04	2.12	0.48	0.19	350	5	333	5.67	16	

UTS: Ultimate tensile strength; EL: elongation-to-failure; ST: solution treatment temperature; St: solution treatment time; ET: extrusion temperature; ES: extrusion speed; ER: extrusion ratio.

0.83 for UTS and EL, respectively, demonstrating its excellent ability in predicting the mechanical properties. The performance of the other models in the order is RF (UTS: 0.87, EL: 0.82), LGBM (UTS: 0.86, EL: 0.79), GB (UTS: 0.85, EL: 0.73), and DT (UTS: 0.78, EL: 0.72). However, LR (UTS: 0.41, EL: 0.29), KNN (UTS: 0.55, EL: 0.44), and MLP (UTS: 0.55, EL: 0.44) models perform less well, with lower R^2 values. Tree-based models (e.g., XGB, RF, LGBM) excel at handling these complex relationships, whereas simple LR and KNN struggle to capture these complexities. This is especially evident in the prediction of EL. This is due to the fact that EL is likely to be affected by more complex factors than UTS, and thus EL is characterized by stronger nonlinearities, and it is difficult for LR, KNN, and MLP to capture these complex nonlinear patterns effectively. Therefore, XGB is subsequently preferred as a forward model.

The hyperparameters of XGB model were tuned using the Bayesian optimization algorithm. The model was run ten times to minimize the likelihood of errors and ensure the reliability of the results. The optimization process of both UTS and EL is shown in [Figure 6C](#). The R^2 values for UTS and EL steadily increase during the initial iterations, indicating that the model is effectively learning and improving its predictions. The UTS exhibits a faster convergence, achieving a higher R^2 of approximately 0.93 after about 70 iterations, reflecting the model's stronger predictive capability for UTS. In contrast, the EL reaches a plateau at a slightly lower R^2 value of around 0.85 after about 100 iterations, showing that while the model is reliable it faces relatively more difficulty in capturing the complex relationships associated with EL.

[Figure 6D](#) and [E](#) highlights the superior performance in predicting UTS and EL after the hyperparameter optimization, respectively. The R^2 value for UTS is 0.99 on the training set, demonstrating an excellent fit between the experimental and predicted data. On the testing set, the R^2 value slightly decreases to 0.93, which still indicates strong generalization capability and reliability in predicting UTS [[Figure 6D](#)]. Similarly, For EL, the R^2 values of 0.98 and 0.86 on the

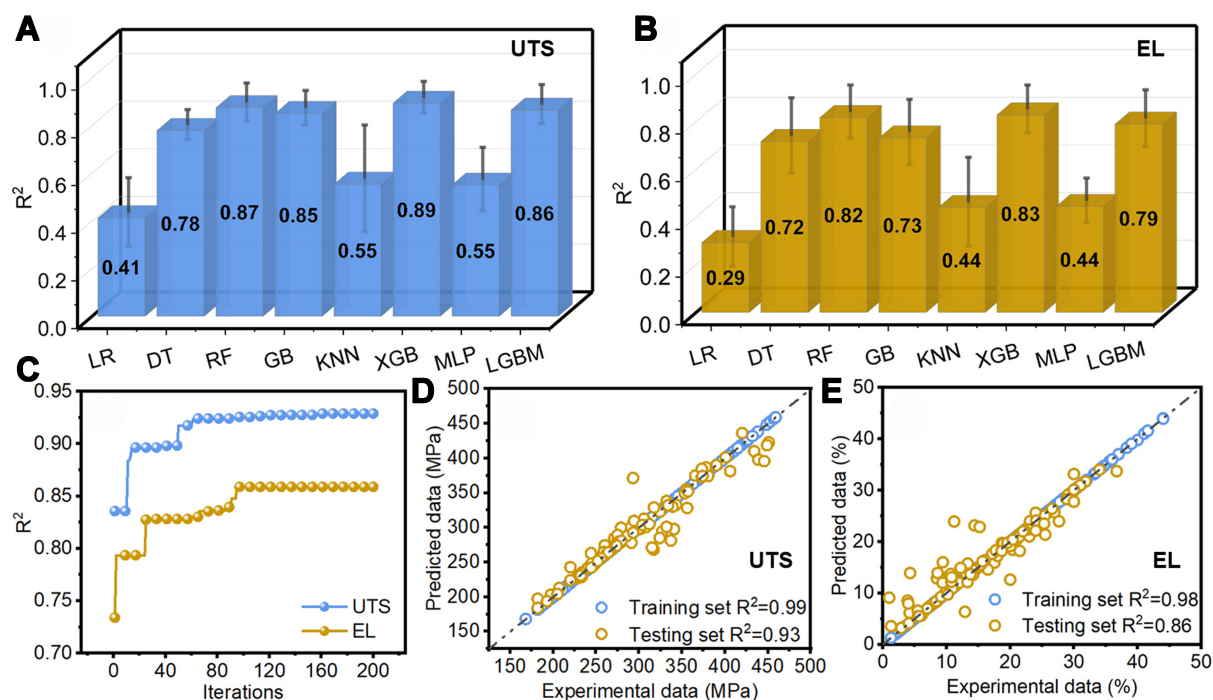


Figure 6. Forward design prediction performance: (A and B) R^2 values of UTS and EL prediction using different models, respectively; (C) hyperparameter optimization process for XGB model; (D and E) prediction accuracy of UTS and EL by XGB model after hyperparameter optimization, respectively. R^2 : The coefficient of determination; UTS: ultimate tensile strength; EL: elongation-to-failure; XGB: XGBoost.

training and the testing sets are achieved, respectively [Figure 6E].

In general, data points from both training and testing sets are more tightly clustered around the ideal prediction diagonal, with R^2 values exceeding 0.90 for UTS and 0.85 for EL. This indicates that the optimized model has high accuracy and reliability for these tasks.

Table 3 presents the results of the forward design predictions for UTS and EL, compared with experimental data. The predictions closely align with the experimental values^[27-31], showcasing the model's strong predictive capability. For example, in A1 alloy, the experimental UTS and EL are 314 MPa and 9.5%, respectively, while the predicted values are 319 MPa and 9.3%, with minimal deviation. Similarly, in A2 alloy, the predicted UTS (427 MPa) and EL (6.9%) are very close to the experimental values of 432 MPa and 7.5%. For A3, A4, and A5 alloys, the differences between prediction and experiment are consistently small, with deviations in UTS ranging from 0 to 5 MPa and in EL from 0.3% to 0.6%. These results demonstrate that the model effectively captures the underlying relationships between composition, processing parameters, and mechanical properties, achieving high accuracy and reliability in the forward design tasks.

However, despite the promising results of the forward design, the ultimate goal in this work is to design new alloys that meet target property requirements. The forward design cannot fully satisfy the property-driven requirements of new alloy development. By combining the forward model with the reverse model, the reverse model helps narrow down the search space of compositions and processing parameters, while the forward model provides more accurate predictions of the mechanical properties for the candidate combinations.

Table 3. Prediction results of forward design model in Al-A5 alloys

Alloy	Al/wt%	Zn/wt%	Ca/wt%	Mn/wt%	ST/°C	St/h	ET/°C	ES/m/min	ER	Category	UTS/MPa	EL/%	Ref.
A1	3.60	0.00	3.40	0.30	0	0	400	0.12	3.60	Experiment	314	9.5	[27]
										Prediction	319	9.3	
A2	3.00	1.00	1.00	0.30	400	24	250	0.10	3.00	Experiment	432	7.5	[28]
										Prediction	427	6.9	
A3	3.00	1.00	0.50	0.30	400	6	300	1.00	9	Experiment	284	22.9	[29]
										Prediction	289	23.2	
A4	4.00	0.00	2.00	0.40	0	0	350	9.40	12	Experiment	314	16.6	[30]
										Prediction	317	16.3	
A5	0.61	0.00	0.46	0.00	400	24	400	3.40	28	Experiment	250	19.4	[31]
										Prediction	250	18.9	

ST: Solution treatment temperature; St: solution treatment time; ET: extrusion temperature; ES: extrusion speed; ER: extrusion ratio; UTS: ultimate tensile strength; EL: elongation-to-failure.

Screening results

Using UTS and EL data within the target property area, 1,000 sets of data were randomly generated as inputs, and the integrated reverse-to-forward model was applied to obtain candidate compositions and processing parameters.

Figure 7 illustrates the screening process for Mg alloys with a good synergy between strength and ductility, which is divided into two main parts: low-alloying screening and SHAP importance analysis. To begin with, parameters that do not meet the low-alloying conditions are excluded, and Equations (7) and (8) are set as boundary conditions. There are 16 candidates including detailed alloy compositions and corresponding process parameters to satisfy both conditions. Subsequently, the SHAP method is applied to further select the most suitable alloy compositions and processing parameters. The top-right section of Figure 7 shows the SHAP distribution plot, where each row represents a feature variable, arranged in descending order of importance. The SHAP values reflect the positive or negative contribution of each feature on the predicted target CPI. Negative values indicate a negative impact on the CPI, while positive values indicate a positive impact. Larger absolute values correspond to greater influence. The color of the points represents the magnitude of the feature values: blue points indicate lower feature values, and red points indicate higher feature values. The bottom-right section of Figure 7 is the feature importance ranking, which quantifies the overall contribution of each feature on the CPI as the numerical value $r(P)$, where P represents the feature. Red bars indicate a positive contribution on the CPI, while blue bars indicate a negative contribution. By ranking the features' contributions, it can be seen that Ca is the most critical parameter affecting the overall mechanical properties of the alloy, showing a negative correlation with $r(P) < 0$. The subsequent parameters in order of contribution are ES (positive impact), Mn (positive impact), ET (negative impact), ER (negative impact), ST (negative impact), Al (negative impact), Zn (positive impact), and St (negative impact). For positively correlated parameters, the maximum value is selected, while for negatively correlated parameters, the minimum value is chosen.

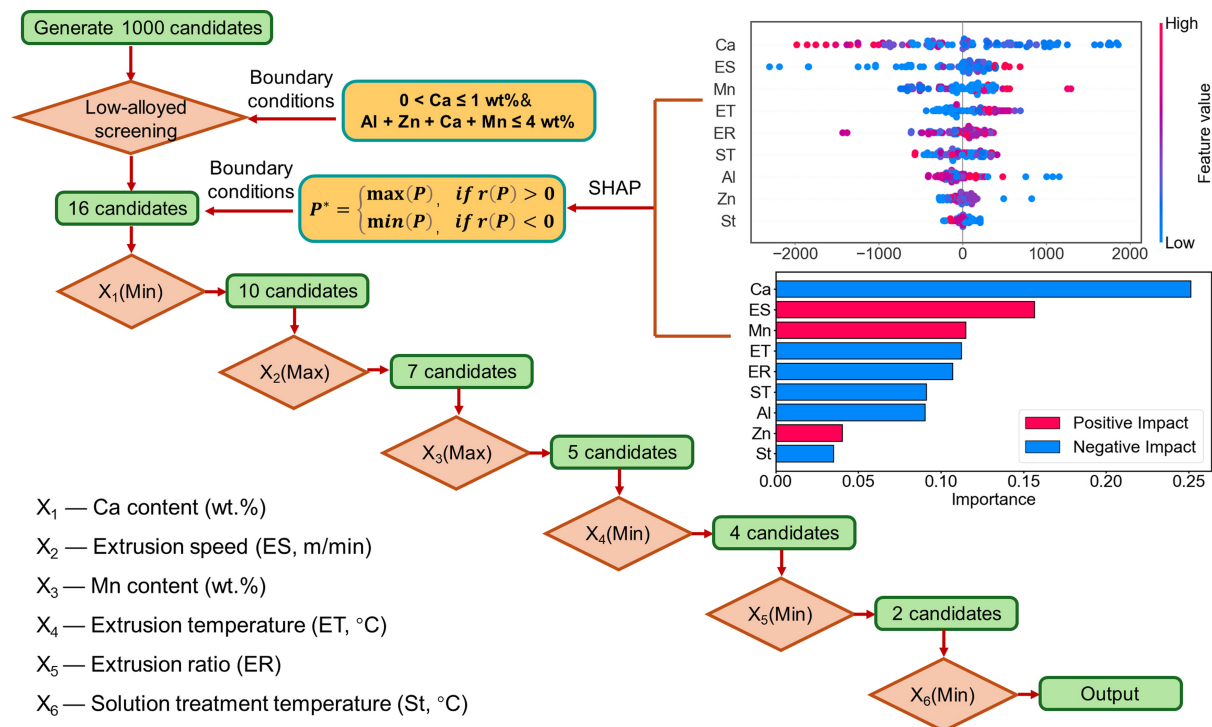


Figure 7. Screening process for low-alloyed Mg alloys with a good synergy between strength and ductility through low-alloying boundary conditions and SHAP importance analysis. SHAP: Shapley Additive Explanations.

Under the guidance of SHAP analysis, as another boundary condition, 16 candidates are further screened. Starting with the most influential parameter, Ca, we determined the minimum value that meets the standard and systematically filtered the remaining parameters in the order (ES, Mn, ET, ER, and ST) indicated by the arrow on the left side of Figure 7. This process ultimately produced 1 candidate with the optimal alloy composition and processing parameters to achieve a good synergy between strength (UTS: 356 MPa) and ductility (EL: 20.3%), as follows: 0.6 wt% Ca, 0.4 wt% Mn, 1 wt% Zn, 2 wt% Al, 20 ER, 400 °C ST, 4 m/min ES, 11 h ST, and 240 °C ET.

Experiment validation

Mechanical properties of new alloy

Based on the mentioned optimal alloy design result, a newly developed Mg-2Al-1Zn-0.6Ca-0.4Mn (AZXM2110, wt%) alloy was prepared through gravity casting, solid-solution treatment, and subsequent extrusion. Figure 8 shows the engineering tensile stress-strain curves of the as-extruded AZXM2110 alloy and the corresponding tensile properties. The average UTS, and EL are about 344 MPa and 21.3%, respectively, which are much closer to the predicted values. The errors between the experimental and predicted values are 3.4% and 5.0% in UTS and EL, respectively. This result indicates well that the POSDD strategy combined with the reverse-to-forward model is a promising approach to guide high-performance low-alloyed Mg alloy design.

Microstructural observation of new alloy

Figure 9A and B demonstrates the SEM image of the as-cast alloy, where some reticular eutectic secondary phases uniformly distribute in the matrix. The chemical compositions of these reticular phases are qualitatively analyzed by element mapping. According to the result of Figure 9C-G, they consist of Mg, Al and Ca elements. After extrusion, the SEM image of the as-extruded alloy is shown in Figure 9H and I,

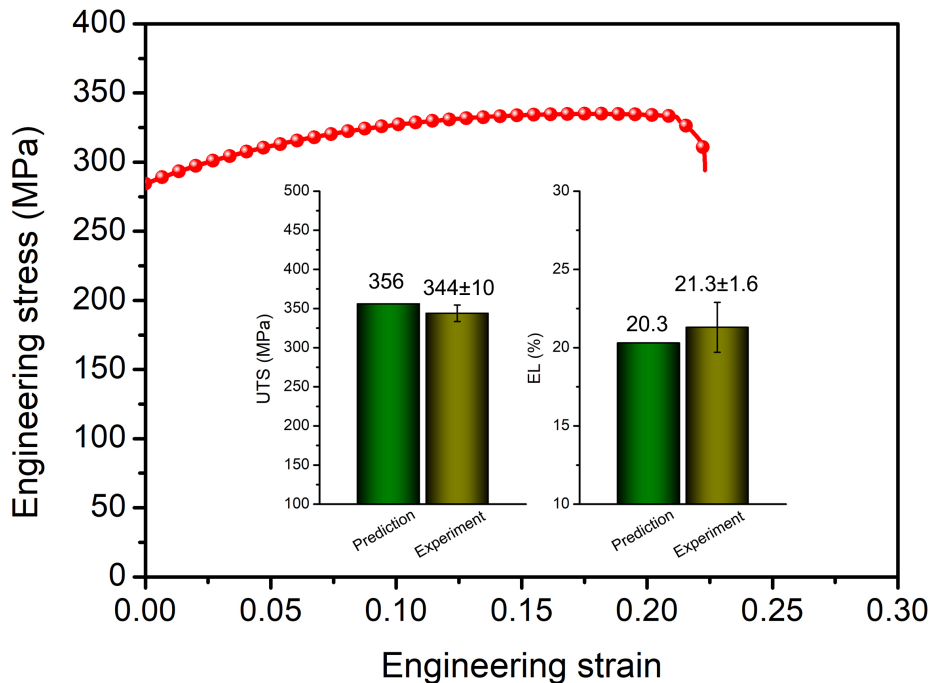


Figure 8. Engineering tensile stress-strain curve of as-extruded alloy and the corresponding mechanical properties (UTS and EL). UTS: Ultimate tensile strength; EL: elongation-to-failure.

where the reticular eutectic secondary phases are fragmented into a number of evenly-distributed granular secondary phases. The average micro-scale phase size of them is about 2.8 μm . Based on the element mapping [Figure 9J-N], herein Mg, Al and Ca elements are still the main chemical compositions.

According to the XRD results of the as-cast and as-extruded alloys [Figure 10], besides the α -Mg phase, there also exists $(\text{Mg,Al})_2\text{Ca}$ phase in both alloys. As reported in the literature^[13,14,30,32], phase compositions are mainly attributed to the types and contents of alloying elements. For example, Li *et al.*^[30] and Yang *et al.*^[32] revealed that Mg-Al-Ca-Mn-(Zn) alloys with Ca/Al mass ratios less than 0.50 included $(\text{Mg,Al})_2\text{Ca}$, while the Ca/Al ratio was greater than 0.90, Mg_2Ca phase was formed. Our observation is highly consistent with their work. In addition, the Al-Mn phase is common in Mg alloys containing Al and Mn elements. However, it is almost not found in the investigated alloy by SEM and XRD results [Figures 9 and 10], because of low Mn content and/or small Al-Mn phase size.

Figure 11A shows the hetero-structured characteristic in the as-extruded alloy by EBSD observation. Such a hetero-structure consists of coarse grains with an average grain size of approximately 16.4 μm and fine grains with an average of about 3.8 μm [Figure 11B]. They account for about 13.8% and 86.2%, respectively. So, the average grain size of the alloy is about 5.5 μm . Figure 11C shows its geometrically necessary dislocation (GND) density distribution map. There is a low GND density of $9.86 \times 10^{13} \text{ m}^{-2}$, since significant dynamic recrystallization (DRX) occurs. Regarding its crystal orientation, this alloy shows a basal fiber texture with $[10\text{-}10]$ components, along with a maximum pole intensity of 6.23 [Figure 11D].

By the observation of TEM, we detect a certain amount of nano-scale granular secondary phases at the grain interiors, whose average phase size is about 19.4 nm [Figure 12A and B]. High-resolution image [Figure 12C] and the corresponding Fast Fourier transformation (FFT) patterns [Figure 12D and E] reveal that phases A and B are $(\text{Mg,Al})_2\text{Ca}$ and Al_8Mn_5 , respectively. However, the area fraction of Al_8Mn_5 phases is

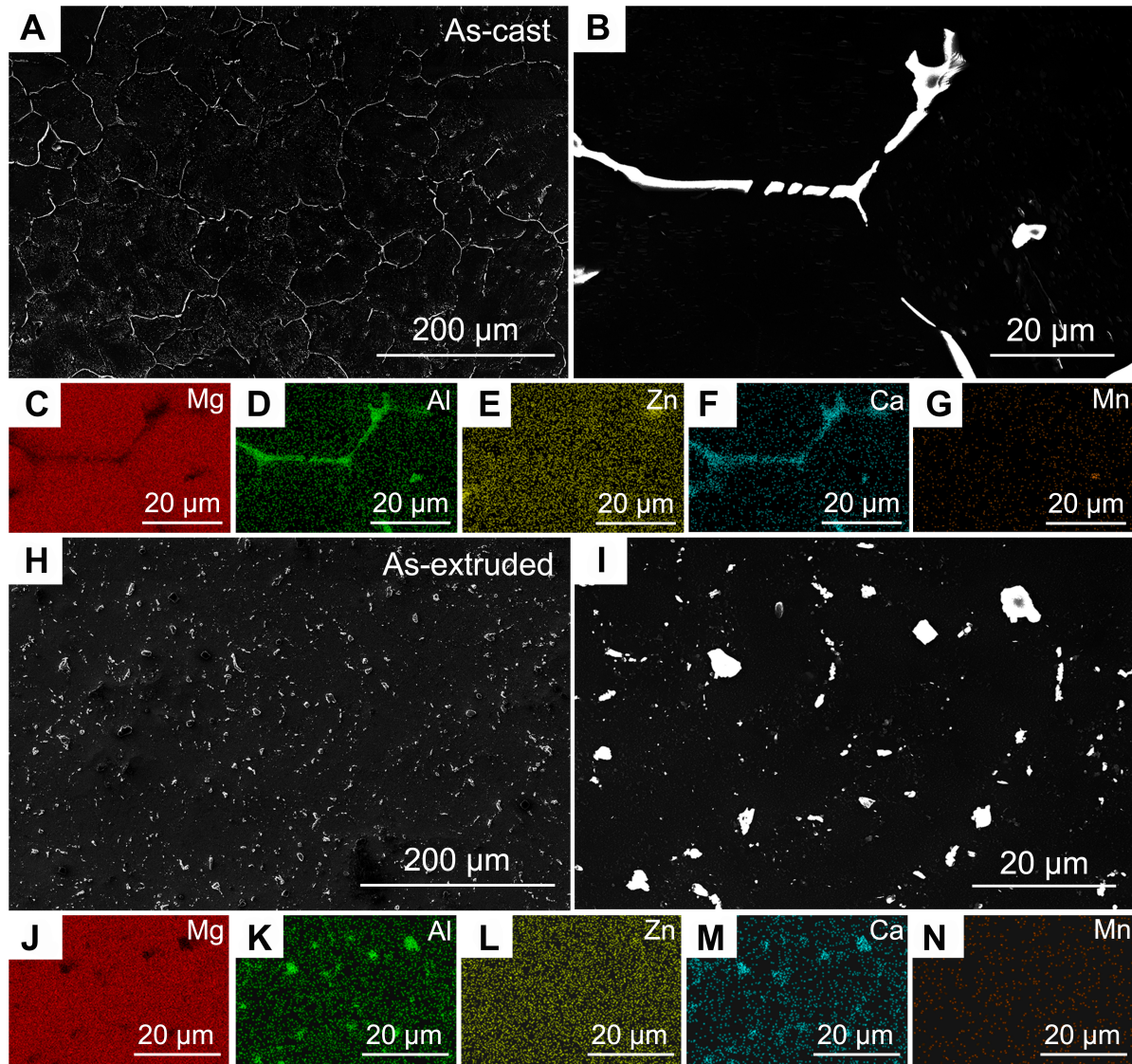


Figure 9. SEM analysis of as-cast and as-extruded alloys: (A and B) SEM image and its high-magnified view and (C-G) element mapping results including Mg, Al, Zn, Ca, and Mn in as-cast alloy; (H and I) SEM image and its high-magnified view and (J-N) element mapping results including Mg, Al, Zn, Ca, and Mn in as-extruded alloy. SEM: Scanning electron microscope.

fairly rare, so they are not measured by SEM and XRD observation.

In addition, as we can see, some nano-scale phases, dispersed at the grain boundaries (GBs), are also found in [Figure 12F-I](#). The relative literature^[33-37] has reported that nano-scale secondary phases, as a double-edged sword, segregated at the GBs play a crucial role in the formation of hetero-structure. In this work, the formation of a large amount of fine grains is not only associated with low ET, but also attributed to the grain boundary-pinning effect of nano-scale phases to a great extent. Owing to the uneven distribution of these nano-scale phases at the GBs, partial GBs migrate during extrusion, resulting in the growth of a few fine grains into coarse grains and the formation of hetero-structure in the as-extruded alloy.

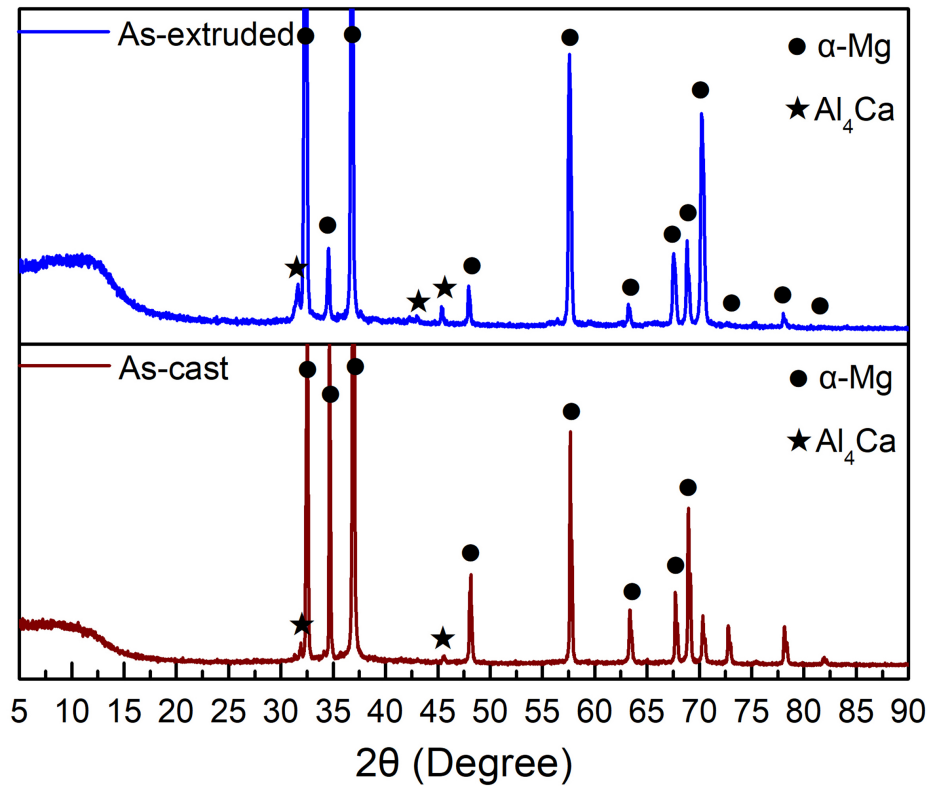


Figure 10. XRD results of as-cast and as-extruded alloys. XRD: X-ray diffraction.

Strengthening mechanisms of new alloy

Generally, it has been widely reported that grain boundary strengthening, secondary phase strengthening, solid-solution strengthening, and dislocation strengthening are common in Mg alloys. In recent years, researchers broadly believe that there is an additional HDI stress in heterogeneous materials during deformation^[38,39], which plays an important strengthening mechanism in further enhancing the strength.

Grain boundary strengthening of the as-extruded alloy can be expressed by Hall-Petch relation as follows^[33]:

$$\sigma_{gb} = \sigma_0 + k \cdot d_{ave}^{-1/2} \quad (10)$$

where σ_{gb} is the contribution of grain boundary on the alloy strength; σ_0 is about the intrinsic strength taken as the UTS of as-cast alloy^[40]; d_{ave} is the average grain size; k is the slope of Hall-Petch relation, which is associated with grain size and texture. In the basal-textured Mg-1.0Ca-1.0Al-0.2Zn-0.1Mn (wt%) alloy, Pan *et al.* reported that k was about 205 MPa/ μm^2 , when grain size exceeded 2 μm ^[41]. In this work, with a similar crystal orientation, the texture effect is considered to be the same as Pan's work. Grain boundary strengthening is calculated to be 146.1 MPa.

Secondary phase strengthening produced by the need for dislocations to by-pass granular-shaped obstacles is given as follows^[42]:

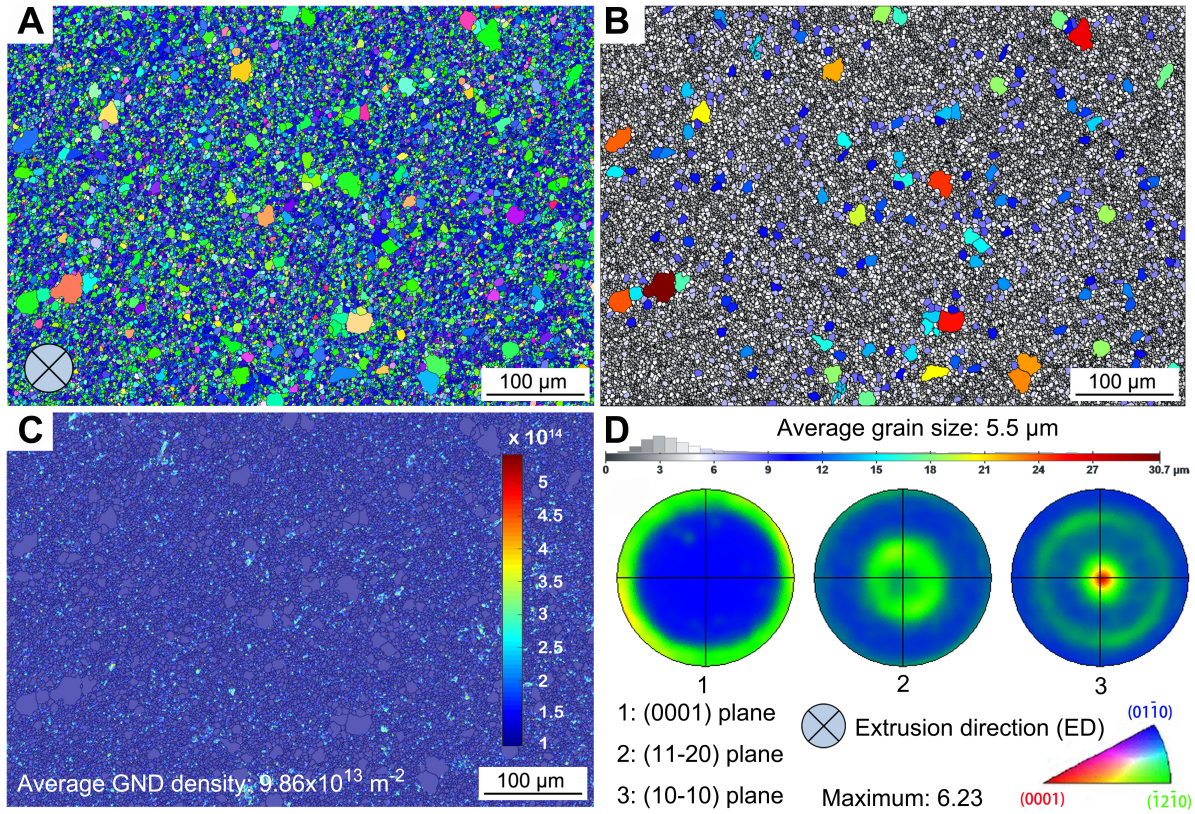


Figure 11. EBSD analysis of as-extruded alloy: (A) Inverse pole figure map, (B) grain size distribution map, (C) dislocation density distribution map, and (D) pole figures including (0001), (11-20), and (10-10). EBSD: Electron backscatter diffraction.

$$\sigma_p = \frac{M G b}{2\pi\sqrt{1-\nu}\left(\frac{0.779}{\sqrt{f_p}} - 0.785\right)d_p} \ln \frac{0.785d_p}{b} \quad (11)$$

where G is the shear modulus of the Mg matrix phase (17 GPa); M is the constant (2.5); b is the magnitude of the Burgers vector of the slip dislocations (0.32 nm); ν is the ratio of Poisson (0.3); f_p and d_p are the area fraction and average phase size of secondary phases, respectively. In the as-extruded MZAX2000 alloy, the f_p and d_p of micro-scale phases are about 1.8% and 2.8 μm ; they are about 0.1% and 19.4 nm for nano-scale phases, respectively. Therefore, the total contribution of micro-/nano-scale phases on the alloy strength is calculated to be 25.2 MPa.

In terms of solid-solution strengthening, generally, it is very finite in low-alloyed wrought alloys due to low content and secondary phase formation. In this work, solid-solution strengthening is ignored.

To assess the contribution of residual dislocations on the alloy strength, dislocation strengthening can be expressed as follows^[43]:

$$\sigma_p = M\alpha G b \sqrt{\rho} \quad (12)$$

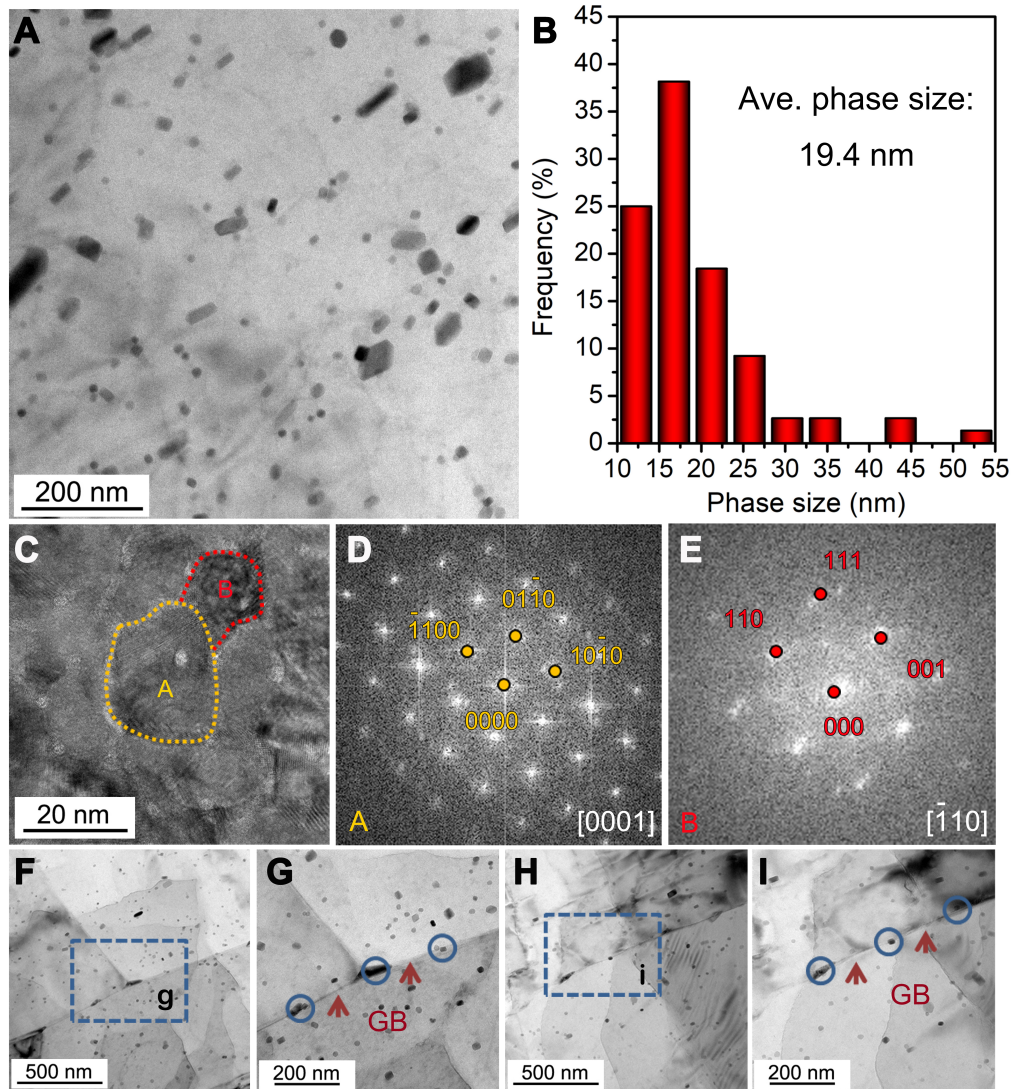


Figure 12. TEM analysis of as-extruded alloy: (A) TEM image showing a certain amount of nano-scale granular-shaped phases; (B) phase size distributions of nano-scale phases; (C) high-resolution TEM image and (D and E) the corresponding FFT patterns of phases A and B, respectively; (F-I) TEM images showing partial nano-scale phases segregated at the GBs. TEM: Transmission electron microscope; FFT: Fast Fourier transformation; GBs: grain boundaries.

where ρ is the dislocation density and α is the constant (0.2). Thus, the contribution of residual dislocations is about 27.1 MPa.

As observed in [Figure 11](#), the as-extruded alloy exhibits a hetero-structure made up of coarse and fine grains. Such a microstructure is also found in Mg-1.0Bi-1.0Mn-1.0Al-0.5Ca-0.3Zn (wt%) alloy (produced by low-speed extrusion and subsequent short-term annealing^[34]) and ZK60 alloy (fabricated by conventional extrusion^[44]). Fu *et al.* reported that the hetero-structured ZK60 alloy had higher UTS than the homogeneous one, increasing by ~23%, owing to the formation of HDI stress^[44]. In this work, the loading-unloading-reloading (LUR) tensile stress-strain curve of the as-extruded alloy is shown in [Figure 13A](#). The LUR curve presents obvious hysteresis loops, as an indicator of HDI stress. As illustrated in [Figure 13B](#), the HDI stress can be calculated by^[38]:

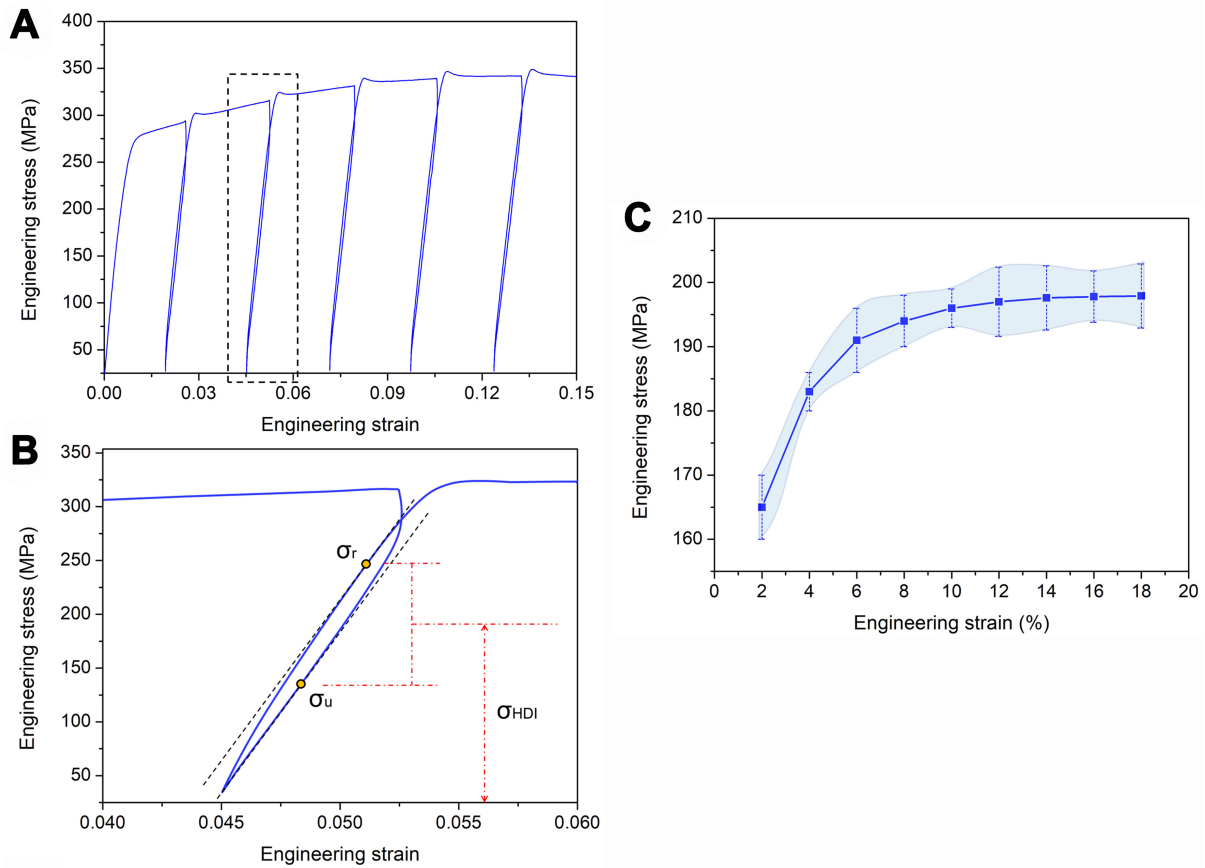


Figure 13. (A) LUR tensile engineering stress-strain curve; (B) Large-magnification view from black dotted box in (A); (C) HDI stress as a function of engineering strain. LUR: Loading-unloading-reloading; HDI: hetero-deformation induced.

$$\sigma_{HDI} = (\sigma_u + \sigma_r)/2 \quad (13)$$

where σ_{HDI} is the HDI stress; σ_u and σ_r represent the unloading and reloading yield stresses, respectively. With the increase of strains from 1% to 18%, the HDI stress continuously reinforces from ~165 to ~197 MPa [Figure 13C], which contributes to a high strain hardening.

Plasticity mechanisms of new alloy

In Mg alloys, basal slip and {10-12} extension twinning are the most common deformation mechanisms due to lower critical resolved shear stresses (CRSSs), in comparison to other deformation modes. Here, {10-12} extension twinning is difficult to activate in such a basal-oriented AZXM2110 alloy along ED-tension, thereby making the contribution of twinning deformation on EL become tiny. Figure 14A and B shows the distribution map of Schmid factor (SF) for basal slip when the as-extruded alloy is applied to tensile load along ED. It can be seen that SF distribution accounts for about 35% at the range from 0.25 to 0.5, because of a weak basal fiber texture including some grains that are conducive to basal slip. The average SF for basal slip is about 0.2, which is beneficial for activating a certain amount of basal dislocations to accommodate strains.

It has also been reported that non-basal slip systems (e.g., pyramidal $\langle c+a \rangle$ slip) are observed in Ca/Li/rare-earth-containing Mg alloys^[45-47]. The additions of these elements alter the stacking fault energy of the Mg

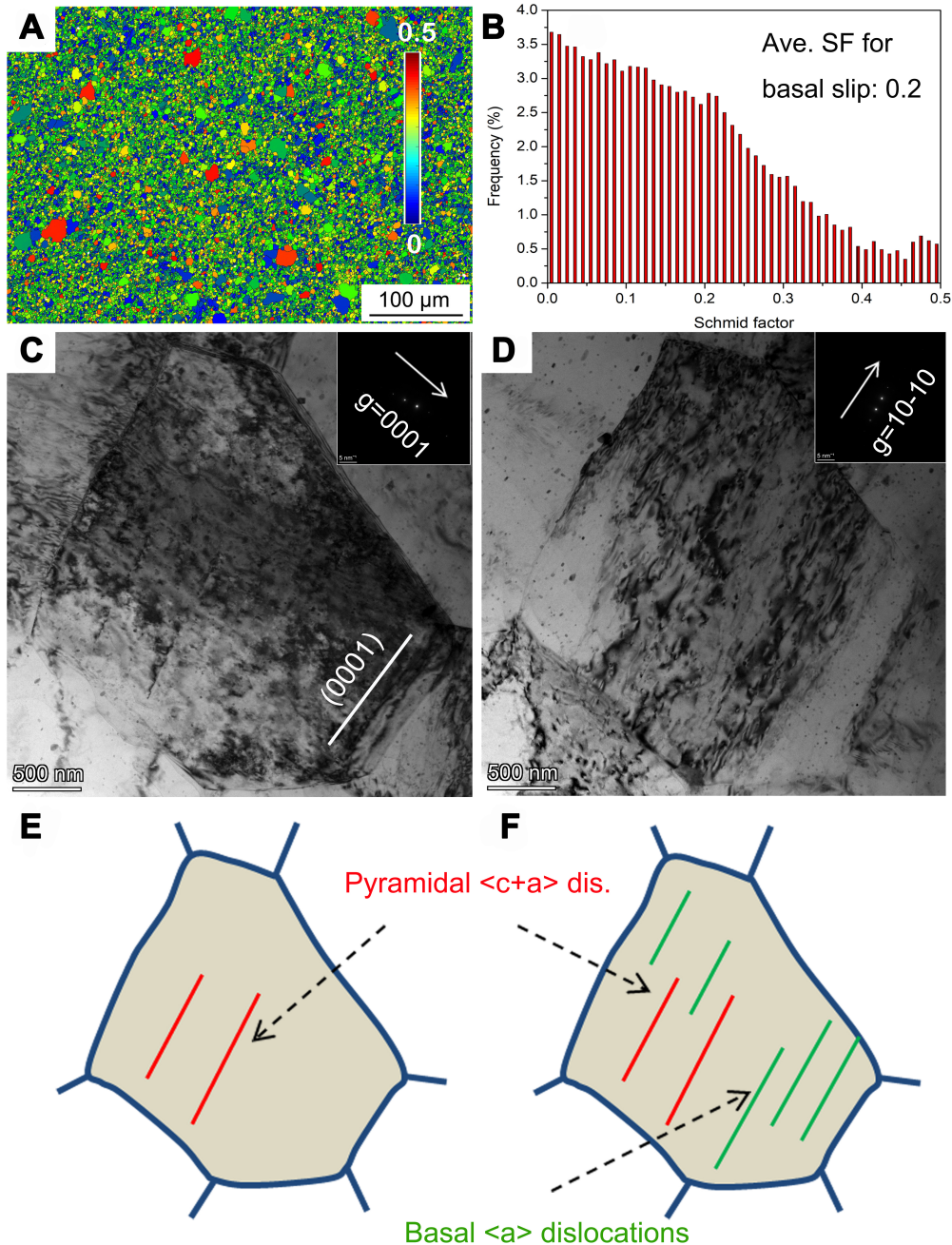


Figure 14. (A and B) SF distribution map for basal slip of as-extruded alloy, when it is applied to tensile load along the ED; (C and D) TEM bright-field images at a tensile strain of 5% using two-beam diffractions under $g = 0001$ and $g = 10-10$, respectively; (E and F) the corresponding schematic diagrams of (C) and (D), respectively. SF: Schmid factor; ED: extrusion direction; TEM: transmission electron microscope.

matrix, making the CRSS ratio between the non-basal and basal slip systems decrease. The non-basal slip activities, to a great extent, provide extra deformation modes to enhance the ductility of the alloy. Figure 14C and D shows the TEM bright-field images of the as-extruded alloy at a tensile strain of 5% using two-beam diffractions under $g = 0001$ and $g = 10-10$, respectively. The $g \cdot b$ (g and b are reciprocal and Burgers vectors, respectively) rule is usually used to judge the types of dislocations^[44]. When the value of $g \cdot b$

is not equal to 0, dislocations are visible. On the contrary, as the value of $g \cdot b$ is equal to 0, it represents the dislocation invisibility. Under $g = 0001$, $\langle a \rangle$ dislocations are invisible due to $g \cdot b = 0$, while $\langle c+a \rangle$ and $\langle c \rangle$ dislocations can be found ($g \cdot b \neq 0$). Under $g = 10\text{-}10$, $\langle c \rangle$ dislocations are disappeared via $g \cdot b = 0$, but partial $\langle a \rangle$ and $\langle c+a \rangle$ dislocations are visible ($g \cdot b \neq 0$). Based on the mentioned rule, pyramidal $\langle c+a \rangle$ dislocations (marked by red lines in Figure 14E and F) and basal $\langle a \rangle$ dislocations (labeled by green lines in Figure 14F) are identified clearly. This result indicates that besides basal $\langle a \rangle$ slip, pyramidal $\langle c+a \rangle$ slip is also involved in tensile deformation. With a similar report, Gu *et al.* found that both basal slip and pyramidal $\langle c+a \rangle$ slip were activated simultaneously in an as-extruded Mg-1Mn-0.5Al-0.5Ca-0.5Zn (wt%) alloy during tension, providing high EL of 19%^[48].

During the plastic deformation of hetero-structured materials, the hetero-zones deform unevenly, generating back stresses in the soft zones and forward stresses in the hard zones, which together produce HDI strain hardening that not only increases the alloy strength, but also enhances its ductility^[35]. Before yielding at 0.2% strain, Frank-Read dislocation source forms in the soft zone interiors, in which GNDs start to pile up the soft/hard zone interface. At this time, the hard zone remains in the elastic stage. With increasing strains, the GNDs located at the interface further accumulate, and continuously propagate in the soft zone interiors to form a GND density gradient. Meanwhile, the opposite hard zone produces the same GND density gradient but a negative strain gradient. Such strain partitioning can produce extra ductility^[34,38,39,44,49]. In the as-extruded alloy, coarse grains provide a higher dislocation storage capacity than fine grains, thereby making coarse and fine grains become soft and hard domains, respectively. It can be confirmed by SF distribution map for basal slip in Figure 14A, where coarse grains exhibit higher SF for basal slip than fine grains. The strain partitioning between the coarse- and fine-grained structure domains is an advantage for the plasticity strain.

CONCLUSIONS

In this work, a POSDD strategy was proposed to excavate high-performance low-alloyed free-RE Mg alloys. The main conclusions were listed as follows:

- (1) The dataset was effectively expanded through the KNN data enhancement method, and the target property area was set based on the Pareto frontier of the current dataset. The integrated reverse-to-forward model was applied to obtain candidate compositions and processing parameters. Combining the low-alloying screening and SHAP importance analysis, the optimal alloy compositions (0.6 wt% Ca, 0.4 wt% Mn, 1 wt% Zn, 2 wt% Al) and processing parameters (20 ER, 400 °C ST, 4 m/min ES, 11 h ST, and 240 °C ET) were excavated to achieve both high strength (UTS: 356 MPa) and high ductility (EL: 20.3%).
- (2) A newly developed AZXM2110 alloy, which was prepared by gravity casting, solid-solution treatment, and subsequent extrusion at given processing parameters, exhibited a hetero-structured characteristic in the as-extruded state consisting of coarse grains (13.8%) and fine grains (86.2%). This alloy achieved a synergy of strength and ductility showing an excellent UTS of 344 MPa and a high EL of 21.3%, which were much closer to the predicted values. This result indicated well that the POSDD strategy was a promising approach to guide high-performance low-alloyed free-RE Mg alloy design.
- (3) In addition to grain boundary strengthening, secondary phase strengthening, and dislocation strengthening, HDI strengthening provided an important contribution to the enhanced UTS. A relatively high SF for basal slip, non-basal slip systems (including pyramidal $\langle c+a \rangle$ slip), and extra strain gradient near the hetero-structured interfaces co-operated the increased EL.

DECLARATIONS

Authors' contributions

Conceptualization, investigation: Qin, X.; Zhao, X.; Xia, S.; Wang, L.; Long, J.

Formal analysis: Qin, X.

Writing-original draft preparation: Qin, X.; Wang, Q.

Project administration: Wang, Q.

Review and editing: Zhang, Y.; Jiang, B.

Availability of data and materials

The data and algorithms used in the current study will be available from the corresponding author based on reasonable request.

Financial support and sponsorship

This research was funded by the National Natural Science Foundation of China (Grant No. 52204407), the Natural Science Foundation of Jiangsu Province (Grant No. BK20220595), and the China Postdoctoral Science Foundation (Grant No. 2022M723689).

Conflicts of interest

All authors declared that there are no conflicts of interest.

Ethical approval and consent to participate

Not applicable.

Consent for publication

Not applicable.

Copyright

© The Author(s) 2025.

REFERENCES

1. Setiawan, D.; Lee, H.; Pyun, J.; et al. Magnesium alloys as alternative anode materials for rechargeable magnesium-ion batteries: review on the alloying phase and reaction mechanisms. *J. Magnes. Alloys*. **2024**, *12*, 3476-90. DOI
2. Zhang, J.; Liu, M.; Qi, J.; et al. Advanced Mg-based materials for energy storage: fundamental, progresses, challenges and perspectives. *Prog. Mater. Sci.* **2025**, *148*, 101381. DOI
3. Yang, H.; Xie, W.; Song, J.; et al. Current progress of research on heat-resistant Mg alloys: a review. *Int. J. Miner. Metall. Mater.* **2024**, *31*, 1406-25. DOI
4. Ovri, H.; Markmann, J.; Barthel, J.; Kruth, M.; Dieringa, H.; Lilleodden, E. T. Mechanistic origin of the enhanced strength and ductility in Mg-rare earth alloys. *Acta. Mater.* **2023**, *244*, 118550. DOI
5. Wei, J.; Wang, Q.; Cai, H.; Ebrahimi, M.; Lei, C. Microstructure and impact behavior of Mg-4Al-5RE-xGd cast magnesium alloys. *J. Magnes. Alloys*. **2024**, *12*, 1799-814. DOI
6. Wang, K.; Wang, X.; Dang, C.; et al. Achieving ultrahigh strength in pre-ageing-extruded Mg-Gd-Y-Zn-Mn alloys via ageing treatment. *J. Mater. Res. Technol.* **2023**, *25*, 7169-79. DOI
7. Huang, Y.; Wan, Y.; Liu, C.; Jiang, S.; Gao, Y.; Chen, Z. Effect of forging temperature on the microstructure, subsequent aging precipitation behavior, and mechanical properties of Mg-Gd-Y-Zr-Ag alloy. *J. Mater. Sci. Technol.* **2024**, *181*, 41-57. DOI
8. Hua, Z.; Li, M.; Wang, C.; et al. Pre-strain mediated fast natural aging in a dilute Mg-Zn-Ca-Sn-Mn alloy. *Scr. Mater.* **2021**, *200*, 113924. DOI
9. Bian, M.; Sasaki, T.; Nakata, T.; et al. Bake-hardenable Mg-Al-Zn-Mn-Ca sheet alloy processed by twin-roll casting. *Acta. Mater.* **2018**, *158*, 278-88. DOI
10. Li, Z. H.; Sasaki, T. T.; Bian, M. Z.; et al. Role of Zn on the room temperature formability and strength in Mg-Al-Ca-Mn sheet alloys. *J. Alloys. Compd.* **2020**, *847*, 156347. DOI
11. Zhai, H.; Wang, L.; Wang, Q.; et al. Achieving high strength near 400 MPa in an ultra-fine grained Mg-Bi-Ca ternary alloy via low-temperature extrusion. *J. Mater. Res. Technol.* **2023**, *26*, 3973-91. DOI

12. Wang, H.; Zhang, D.; Qiu, C.; Zhang, W.; Chen, D. Achieving superior strength-ductility synergy in a heterostructured magnesium alloy via low-temperature extrusion and low-temperature annealing. *J. Mater. Sci. Technol.* **2023**, *163*, 32-44. DOI
13. Liu, X.; Qiao, X.; Pei, R.; Chi, Y.; Yuan, L.; Zheng, M. Role of extrusion rate on the microstructure and tensile properties evolution of ultrahigh-strength low-alloy Mg-1.0Al-1.0Ca-0.4Mn (wt.%) alloy. *J. Magnes. Alloys.* **2023**, *11*, 553-61. DOI
14. Zhang, J.; Peng, P.; Yang, Q.; Luo, A. A. Bimodal grain structure formation and strengthening mechanisms in Mg-Mn-Al-Ca extrusion alloys. *J. Magnes. Alloys.* **2023**, *11*, 4407-19. DOI
15. Huo, P. D.; Li, F.; Xu, H. Y.; Niu, W. T.; Gao, R. H. Achieving large-scale gradient structure in the AZ31 magnesium alloys for extraordinary strength-ductility synergy by hard plate rolling. *J. Alloys. Compd.* **2023**, *944*, 169176. DOI
16. Thanabal, N.; Silambarasan, R.; Seenuvasaperumal, P.; Basha, D. A.; Elayaperumal, A. Microstructure and mechanical behavior of AXM Mg alloy systems - a review. *J. Magnes. Alloys.* **2024**, *12*, 2624-46. DOI
17. Lee, J.; Kim, M.; Lee, Y. Design of high strength medium-Mn steel using machine learning. *Mater. Sci. Eng. A.* **2022**, *843*, 143148. DOI
18. Li, X.; Zheng, M.; Pan, H.; Mao, C.; Ding, W. An integrated design of novel RAFM steels with targeted microstructures and tensile properties using machine learning and CALPHAD. *J. Mater. Inf.* **2024**, *4*, 27. DOI
19. Yuan, Y.; Sui, Y.; Li, P.; Quan, M.; Zhou, H.; Jiang, A. Multi-model integration accelerates Al-Zn-Mg-Cu alloy screening. *J. Mater. Inf.* **2024**, *4*, 23. DOI
20. Qin, X.; Zhai, H.; Wang, L.; Xia, S.; Jiang, B.; Wang, Q. A novel multimodal feature fusion convolutional neural network to predict the mechanical properties of magnesium alloys. *Mater. Lett.* **2024**, *370*, 136863. DOI
21. Hairani, H.; Widiyaningtyas, T.; Dwi, P. D. Addressing class imbalance of health data: a systematic literature review on modified synthetic minority oversampling technique (SMOTE) strategies. *JOIV. Int. J. Inform. Vis.* **2024**, *8*, 1310. DOI
22. Low, A. K.; Vissol-gaudin, E.; Lim, Y.; Hippalgaonkar, K. Mapping pareto fronts for efficient multi-objective materials discovery. *J. Mater. Inf.* **2023**, *3*, 11. DOI
23. Wang, Q.; Qin, X.; Xia, S.; et al. Interpretable machine learning excavates a low-alloyed magnesium alloy with strength-ductility synergy based on data augmentation and reconstruction. *J. Magnes. Alloys.* **2025**, *In Press*. DOI
24. Habeb, A. A. A.; Taresh, M. M.; Li, J.; Gao, Z.; Zhu, N. Enhancing medical image classification with an advanced feature selection algorithm: a novel approach to improving the cuckoo search algorithm by incorporating caputo fractional order. *Diagnostics* **2024**, *14*, 1191. DOI PubMed PMC
25. Zhang, W.; Li, P.; Wang, L.; et al. Prediction of the yield strength of as-cast alloys using the random forest algorithm. *Mater. Today. Commun.* **2024**, *38*, 108520. DOI
26. Jiang, L.; Wang, C.; Fu, H.; Shen, J.; Zhang, Z.; Xie, J. Discovery of aluminum alloys with ultra-strength and high-toughness via a property-oriented design strategy. *J. Mater. Sci. Technol.* **2022**, *98*, 33-43. DOI
27. Xu, S.; Oh-ishi, K.; Kamado, S.; Takahashi, H.; Homma, T. Effects of different cooling rates during two casting processes on the microstructures and mechanical properties of extruded Mg-Al-Ca-Mn alloy. *Mater. Sci. Eng. A.* **2012**, *542*, 71-8. DOI
28. Zeng, Z. R.; Zhu, Y. M.; Nie, J. F.; Xu, S. W.; Davies, C. H. J.; Birbilis, N. Effects of calcium on strength and microstructural evolution of extruded alloys based on Mg-3Al-1Zn-0.3Mn. *Metall. Mater. Trans. A.* **2019**, *50*, 4344-63. DOI
29. Song, L.; Lu, Y.; Zhang, Y.; Li, X.; Cong, M.; Xu, W. The effect of Ca addition on microstructure and mechanical properties of extruded AZ31 alloys. *Vacuum* **2019**, *168*, 108822. DOI
30. Li, Z.; Zhang, X.; Zheng, M.; et al. Effect of Ca/Al ratio on microstructure and mechanical properties of Mg-Al-Ca-Mn alloys. *Mater. Sci. Eng. A.* **2017**, *682*, 423-32. DOI
31. Jiang, Z.; Jiang, B.; Yang, H.; Yang, Q.; Dai, J.; Pan, F. Influence of the Al₂Ca phase on microstructure and mechanical properties of Mg-Al-Ca alloys. *J. Alloys. Compd.* **2015**, *647*, 357-63. DOI
32. Yang, A.; Nie, K.; Deng, K.; Li, Y. Improved tensile properties of low-temperature and low-speed extruded Mg- χ Al-(4.8- χ)Ca-0.6Mn alloys. *J. Mater. Res. Technol.* **2020**, *9*, 11717-30. DOI
33. Zhang, Z.; Xia, S.; Chen, X.; et al. Achieving ultra-high extrusion speed and strength-ductility synergy in a BAZ531 magnesium alloy via differential-thermal extrusion. *Mater. Sci. Eng. A.* **2025**, *923*, 147687. DOI
34. Xiao, Z.; Xu, S.; Huang, W.; et al. Unexpected effects on creep resistance of an extruded Mg-Bi alloy by Zn and Ca co-addition: experimental studies and first-principles calculations. *J. Mater. Sci. Technol.* **2024**, *201*, 166-86. DOI
35. Peng, P.; He, X.; She, J.; et al. Novel low-cost magnesium alloys with high yield strength and plasticity. *Mater. Sci. Eng. A.* **2019**, *766*, 138332. DOI
36. Jiang, C.; Lu, B.; Pan, H.; et al. Effect of Al addition on microstructure and mechanical property of Mg-Mn-Ca-Ce based alloy. *J. Alloys. Compd.* **2024**, *1005*, 175975. DOI
37. Zhang, W.; Shen, Z.; Pan, H.; et al. Enhancing strength and irradiation tolerance of Mg alloy via co-addition of Mn and Ca elements. *J. Mater. Sci. Technol.* **2025**, *216*, 38-51. DOI
38. Zhu, Y.; Ameyama, K.; Anderson, P. M.; et al. Heterostructured materials: superior properties from hetero-zone interaction. *Mater. Res. Lett.* **2021**, *9*, 1-31. DOI
39. Chen, X.; Zhang, J.; Wang, M.; et al. Research progress of heterogeneous structure magnesium alloys: a review. *J. Magnes. Alloys.* **2024**, *12*, 2147-81. DOI
40. Liu, C.; Chen, X.; Chen, J.; Atrens, A.; Pan, F. The effects of Ca and Mn on the microstructure, texture and mechanical properties of Mg-4 Zn alloy. *J. Magnes. Alloys.* **2021**, *9*, 1084-97. DOI

41. Pan, H.; Kang, R.; Li, J.; et al. Mechanistic investigation of a low-alloy Mg–Ca-based extrusion alloy with high strength–ductility synergy. *Acta Mater.* **2020**, *186*, 278-90. [DOI](#)
42. Nie, J. Effects of precipitate shape and orientation on dispersion strengthening in magnesium alloys. *Scr. Mater.* **2003**, *48*, 1009-15. [DOI](#)
43. Lan, Y.; Jia, M. Multiple strengthening mechanisms of grain/twin boundaries, dislocations and nanoprecipitates in Mg alloys induced by laser shock processing. *Mater. Today. Commun.* **2024**, *38*, 107645. [DOI](#)
44. Fu, W.; Dang, P.; Guo, S.; et al. Heterogeneous fibrous structured Mg–Zn–Zr alloy with superior strength-ductility synergy. *J. Mater. Sci. Technol.* **2023**, *134*, 67-80. [DOI](#)
45. Xu, J.; Guan, B.; Xin, Y.; et al. The mechanism for Li-addition induced homogeneous deformation in Mg-4.5wt.% Li alloy. *Inter. J. Plast.* **2023**, *170*, 103763. [DOI](#)
46. Wu, Z.; Ahmad, R.; Yin, B.; Sandlöbes, S.; Curtin, W. A. Mechanistic origin and prediction of enhanced ductility in magnesium alloys. *Science* **2018**, *359*, 447-52. [DOI](#) [PubMed](#)
47. Zhu, G.; Wang, L.; Zhou, H.; et al. Improving ductility of a Mg alloy via non-basal <a> slip induced by Ca addition. *Int. J. Plast.* **2019**, *120*, 164-79. [DOI](#)
48. Gu, G.; Ke, X.; Hu, F.; et al. Fine-grained Mg–1Mn–0.5Al–0.5Ca–0.5Zn alloy with high strength and good ductility fabricated by conventional extrusion. *Trans. Nonferrous. Met. Soc. China.* **2022**, *32*, 483-92. [DOI](#)
49. Ji, W.; Zhou, R.; Vivegananthan, P.; See, W. M.; Gao, H.; Zhou, K. Recent progress in gradient-structured metals and alloys. *Prog. Mater. Sci.* **2023**, *140*, 101194. [DOI](#)